Materials Reports: Energy 3 (2023) 100196

Contents lists available at ScienceDirect

Materials Reports: Energy

journal homepage: www.keaipublishing.com/en/journals/materials-reports-energy

Original Research Report

Selective conversion of CO_2 to CO using earth abundant tin modified copper gas diffusion electrodes

Preetam K. Sharma [a], Shahid Rasul [b], Da Li [c], Eileen H. Yu [a,*]

[a] Department of Chemical Engineering, Loughborough University, Loughborough, LE11 3TU, UK
[b] Faculty of Engineering and Environment, Northumbria University, Ellison Pl, Newcastle Upon Tyne, NE1 8ST, UK
[c] State Key Laboratory of Urban Water Resource and Environment, School of Environment, Harbin Institute of Technology, Harbin, 150090, China

ARTICLE INFO

Keywords:
Electrochemical CO_2 reduction
Cu–Sn binary Catalyst
Optimising loading
Selective CO production
Surface reconstruction

ABSTRACT

Earth-abundant copper-tin (CuSn) electrocatalysts are potential candidates for cost-effective and sustainable production of CO from electrochemical carbon dioxide reduction (eCO_2R). However, the requirement of high-overpotential for obtaining reasonable current, low Faradaic efficiencies (FE) and low intrinsic catalytic activities require the optimisation of the CuSn nanoarchitecture for the further advancement in the field. In the current work, we have optimised Sn loading on Cu gas diffusion electrodes (GDEs) by electrochemical spontaneous precipitation. Samples with various Sn loadings were tested in a three-chamber GDE reactor to evaluate their CO_2 reduction performances. The best performance of 92% CO Faradaic efficiency at a cathodic current density of 120 mA cm^{-2} was obtained from the 20 min Sn deposited Cu_2O sample operated at −1.13 V vs. RHE. The electrocatalyst had ~13% surface coverage of Sn on Cu GDE surface, and had Sn in oxide form and copper in metallic form. The catalyst also showed stable performance and was operable for >3 h under chronoamperometric conditions. The surface of the GDE reduces from Cu_2O to Cu during eCO_2R and goes further reconstruction during the eCO_2R. This study demonstrates the potential of Cu–Sn for selective CO production at high current densities.

1. Introduction

Carbon dioxide (CO_2) is a major greenhouse gas which is driving the climate change. CO_2 capture at the emission sources and from air followed by conversion to fuels/chemicals can achieve carbon neutral energy cycle.[1] Electrochemical CO_2 reduction (eCO_2R) is one of the most promising methods for the direct production of fuels and chemicals from CO_2 and water.[2,3] With electrical energy supplied by a renewable sources and oxygen as the by-product at the anode, eCO_2R can be environmentally friendly and sustainable. However, several issues including low current density, catalyst instability, poor product selectivity and carbon loss as carbonate hinder practical applications of the process.[4,5] In this study, we worked on improving selectivity towards carbon monoxide (CO) in a three-chamber GDE reactor. The reactor has been shown to deliver higher current than traditional H-cell due to enhanced CO_2 mass transport.[6]

CO is a valuable chemical feedstock which can be converted to methanol via hydrogenation and liquid hydrocarbons using established industrial methods like Fischer-Tropsch process.[7,8] Due to its inherent simplicity ($2e^-$ transfer), profitability and potential for further utilisation by electrochemical or chemical methods, CO_2 to CO conversion can also be a good target for scale-up experiments.[9–11] However, the requirement of noble metal (such as Ag, Au and Pd) electrodes, make the process less economically attractive.[12,13] Therefore, there is a need of developing catalysts free of noble metals. Carbon materials have delivered promising results in terms of Faradaic efficiencies (FE) but have not been able to deliver desired CO FE at higher current densities (>50 mA cm^2).[14–16] Therefore, non-binary metals-based nano-catalysts in alloy, hetero-structure and surface modified structures have been explored for obtaining sustainable and cost-effective catalysts with enhanced performances.[17–20]

* Corresponding author.
E-mail address: e.yu@lboro.ac.uk (E.H. Yu).

Production and Hosting by Elsevier on behalf of KeAi

https://doi.org/10.1016/j.matre.2023.100196
Received 15 February 2023; Received in revised form 26 March 2023; Accepted 31 March 2023
Available online 18 April 2023

Bimetallic electrodes based on copper and tin (Cu–Sn) have shown some promising results in terms of selectivity for CO production.[21,22] The results are different from either of Cu and Sn based catalysts which are known for producing higher carbons and formate, respectively.[23,24] In our previous work, Sn modified Cu metallic foil demonstrated a CO FE of 91% at 1.0 V vs. RHE in an H-cell.[22] Sarfraz et al. electrodeposited Sn on oxide derived Cu sheet and utilised it for determining CO_2 reduction performance in a two-chamber reactor.[21] They obtained >90% CO FE and 3 mA cm^{-2} cathodic current density at −0.8 V vs. RHE. In another study, Perez et al. investigated the atomic layer deposited Sn on the top of $Cu(OH)_2$ nanowires and obtained 3.2 mA cm^{-2} current density and 77% selectivity towards CO at −0.7 V vs. RHE.[18] They, by a combination of in-situ X-ray absorption spectroscopy, X-ray photoelectron spectroscopy, and density functional theory calculations, determined the optimal Sn content on the surface to be 13%. Beyond 45% surface coverage of Sn, their system behaved similar to pure Sn electrode and produced formate, selectively.

A variety of reactor architectures have been explored using Cu–Sn for selective conversion of CO_2 to CO. Most of the early investigations on Cu–Sn electrocatalysts were carried out using a standard H-cell where cathode and anode chambers are separated by a membrane.[25–27] The advantage of H-cell lies in its robustness and simple architecture. Gao et al. employed a two-chamber flow reactor using Cu–Sn electrode in $KHCO_3$ electrolyte to obtain 180 mA cm^{-2} current at 0.9 V cathodic potential with >83% Faradaic efficiency of CO.[28] Due to the poor solubility of CO_2 in water, low current densities of <20 mA cm^{-2} were obtained in most of the reports (Table S2, ESI). This motivated the researcher to explore three-chamber GDE cells. In the GDE cells, the mass transport of CO_2 to the catalyst surface is significantly improved. For instance, Tan et al. obtained 265 mA cm^{-2} partial CO current density with >90% FE using co-precipitated Cu/Sn electrodes.[29] The researchers utilised anion exchange membrane to separate the cathode and anode chambers. However, anion exchange membrane can allow liquid products like formate to pass through, which can lead to inaccurate estimation of the Faradaic efficiency of the products. In the current work, we have utilised a cation exchange membrane which should provide a more accurate estimate of the produced formate by containing products on the cathode side. The issue of reactor flooding and mass-transport losses encouraged researchers to explore fuel cell type MEA (membrane-electrode assembly) reactors, also known as zero-gap cells. Ju et al. were able to obtain 125 mA cm^{-2} current with >80% CO FE at −1.2 V in a MEA cell. They also demonstrated the stability of performance for over 130 h.[30]

In this work, a series of Cu–Sn samples were prepared via surface modification of Cu_2O GDE by Sn using electrochemical spontaneous precipitation (ESP). Thereafter, the eCO_2R performances of the catalysts were evaluated in a three-chamber GDE cell. The activity assessment was performed at −1.13 V vs. RHE to determine the electrocatalyst with optimal Sn deposition time for further analysis. The best sample was utilised for determining the activity at various potentials and stability of the electrodes in the three-chamber reactor configuration. A variety of characterisation techniques were applied for determining the changes in the catalysts before and after the eCO_2R, which further contributes to understanding the changes in catalyst composition, surface species, structure and reaction mechanism.

2. Experimental section

2.1. Preparation of Cu_2O GDE

The preparation of Cu_2O GDEs has been reported in our previous work.[6] In brief, 15 mg commercial Cu_2O catalysts were sonicated in 200 μL (99.5%, Sigma-Aldrich) isopropanol. After 10 min, 33 μL Nafion binder (5 wt%, Sigma-Aldrich) was added. The catalyst ink was then sonicated for 1 h before layer-by-layer painting onto a 2 cm^2 surface area of carbon gas diffusion layer (H2315 I2 C6, Freudenberg). The GDEs were dried between coats at 50 °C for 2 min. The final loadings of the catalyst on GDEs were ~5 mg cm^2. The samples were dried at 50 °C for 30 min before employing for eCO_2R. SnO_2 GDEs were also prepared by starting with 15 mg SnO_2 nanoparticles following the above protocol.

2.2. Preparation of Cu–Sn GDE

ESP of Sn on Cu GDEs was performed using Cu_2O GDEs and Sn foil electrodes in an electrolyte comprising 0.1 M $SnCl_4{\cdot}5H_2O$ and 0.05 M citric acid.[22] The solution was stirred well to ensure dissolution of Sn salt. The ESP was performed at room temperature on a stirrer with both the electrodes connected by an external wire. The effect of the reaction time was investigated by depositing Sn in 5–60 min. Accordingly, the samples of Sn modified Cu_2O GDE were named using the convention $CuSn_{5\_min}$, $CuSn_{10\_min}$ and so on.

2.3. Electrochemical CO_2 reduction measurements

eCO_2R measurements were performed in a three-chamber GDE cell in a three-electrode mode. The details of the cell structure and assembly are provided in our previous work.[17] The current set-up consists of GDE as working electrode, Pt coated Ti mesh as counter electrode, and Hg/HgO (RE-5B, BASI, 1 M KOH, 0.118 V vs. RHE) as reference electrode. 1 M KOH was utilised as catholyte, and 5 M KOH was used as anolyte. The electrolyte chambers were separated by a cation exchange membrane (F-1050, Fumapem) to stop the cross-over of the liquid products. Cyclic voltammetry measurements were conducted on fresh samples in the presence of N_2 and CO_2 gases (flow rate 15 sccm) sequentially in −1.05 to +0.95 V vs. RHE. The chronoamperometric measurements for various samples at various potentials were taken in the reactor in batch mode. For determining the stability of the GDE electrode, the reactor was operated in flow-mode, connected to an electrolyte reservoir, for enabling the collection of liquid samples at regular intervals. Pure CO_2 gas (99.9995% purity, BOC) flow was controlled via a Bronkhorst digital mass flow controller and maintained at 15 mL min^{-1} for the measurements.

The potentials in the current work have been reported vs. RHE, according to Equation (1).

$$E\ (\text{vs. RHE}) = E\left(vs\,\frac{\text{Hg}}{\text{HgO}}\right) + 0.118 + 0.0591 \times \text{pH} + iR \quad (1)$$

The samples were analysed in the potential range of −0.55 to −1.35 V vs. RHE range to determine the effect of overpotential. The resistance measured in GDE cell at high frequency (1×10^5 Hz) and at 10 mV RMS amplitude by electrochemical impedance spectroscopy was around 0.1 Ω. The resistance value was utilised to calculate the *iR* drop at various currents.[31]

The current densities were determined by dividing the obtained current by the GDE area of 2 cm^2. The current densities in text are described as cathodic current density and without any negative sign.

2.4. Product yield and Faradaic efficiency calculations

The CO_2 reduction products were analysed by gas and ion chromatographic techniques. The gaseous products were measured by online gas chromatography using ShinCarbon Micropacked Column (Shimadzu Nexis GC-2030) where the outlet of the gas chamber was directly connected with the injection port of GC for taking out samples at regular intervals. The liquid products were analysed manually after the collection. Alcohols were detected by GC (Shimadzu Nexis GC-2030, DB-Wax column), and organic acids were analysed by ion chromatography (Eco IC, Metrohm).

The Faradaic efficiency describes the fraction of current used for generating a particular product, represented by Equation (2).

$$FE = \frac{znF}{Q} \quad (2)$$

Where, Q is the total charge passed, F is Faraday's constant (96,485 C mol^{-1}), z is the number of electrons required per mole of product, and n is moles of products generated. The total Faradaic efficiency for samples ranged from 80% to 101%. Several factors could affect the total Faradaic efficiency values including the side reaction of catalyst reduction along with the CO_2 reduction process, cross-over of gaseous products via the GDE and membrane, and averaging the obtained current. The issue with averaging the current is that liquid products get accumulated over a period of time, which should have been correctly identified. However, the gaseous products are injected in GC at particular instances/time-points, leading to the possibility of not accounting for the actual current. The obtained Faradaic efficiency values for the samples are reported in Table S3. Total Faradaic efficiencies were normalised to 100% to have a direct comparison between different samples.

Energy efficiency for the overall reactor was determined by multiplying the full-cell voltage efficiency with product Faradaic efficiency. The measured full-cell voltage at −1.13 V and −120 mA cm^{-2} for the $CuSn_{20\_min}$ GDE reactor is 2.7 V.

2.5. Materials characterisation

X-ray diffraction (XRD) analysis was carried out on a Bruker D2 phaser benchtop X-ray diffractometer using Cu K_α radiation source (λ: 1.5406 Å) in 2θ range of 10–80°. Elemental composition and chemical valence states analysis was completed by X-ray photoelectron spectroscopy (XPS) using a Thermo Scientific K-Alpha instrument with Al K_α X-ray (1486.6 eV) source on 400 × 400 μm^2 spot size. The energy calibration was performed by using C 1s peak at 284.8 eV. Scanning electron microscope (SEM) (Jeol JSM 7100 F FEGSEM) was used to analyse the morphology of the materials. The elemental analysis was carried out using Oxford instruments energy dispersive X-ray (EDS) detector coupled with the SEM at 10 kV accelerating voltage. The samples were coated with a thin layer of Au–Pd before loading in the SEM chamber to enhance the conductivity.

3. Results and discussion

3.1. Cu–Sn synthesis and effect of Sn deposition time

3.1.1. Mechanism of the Sn deposition on Cu_2O GDE

The ESP of Sn on Cu_2O GDE was carried out in acidic Sn^{4+} solution using Cu_2O GDE and Sn metal electrodes. The mechanism of Sn ESP is very similar to the ESP of In on Cu_2O GDE, discussed in detail previously.[17] Based on the standard reduction potentials for the Sn and Cu species, the following mechanism of the electrochemical surface modification of the GDE is proposed.

Anode reaction, which takes place on Sn metal electrode ($E^o = -0.13$ V)

$$Sn \rightarrow Sn^{2+} + 2e^- \quad (3)$$

Cathode reaction, which takes place on Cu_2O GDE electrode ($E^o = 0.463$ V)

$$Cu_2O + 2e^- + 2H^+ \rightarrow 2Cu + H_2O \quad (4)$$

The deposition of Sn takes place locally by the precipitation of $Sn(OH)_4$ on the surface of Cu_2O GDE. Upon enhancement of local pH due to CuO_x reduction, the additional hydroxides get consumed by Sn^{4+}, which leads to the production of $Sn(OH)_4$. $Sn(OH)_4$ readily converts to Sn oxide in ambient conditions as shown in Equation (5).

$$Sn^{4+} + 4OH^- \rightarrow Sn(OH)_4 \rightarrow SnO_2 \quad (5)$$

3.1.2. Physicochemical investigations of the prepared catalysts

The change in the crystalline nature of $CuSn_{20\_min}$ before and after 1 h of eCO_2R at −1.13 V was determined using XRD, shown in Fig. 1a. The diffractograms of Cu_2O and SnO_2 GDE electrodes are also shown for reference. The diffractogram of Cu_2O GDE and $CuSn_{20\_min}$ (best sample for electrochemical CO production, discussed later in the section) is very different, where without surface restructuring there should have been some additional peaks corresponding to Cu_2O species. However, it is observed that fresh $CuSn_{20\_min}$ has predominantly Cu metallic phase as compared to the Cu_2O which is mostly Cu_2O with a small contribution of CuO. The reduction of Cu during ESP has also been observed in our previous work.[17] No peaks corresponding to Sn species were identified. This indicates that Sn layer is very thin on the surface or Sn is deposited as amorphous clusters. After undergoing eCO_2R, the small peak corresponding to Cu_2O gets even smaller, indicating further reduction of the Cu on the GDE surface. The values of full-width at the half-maximum of the XRD peaks vary between the samples. Therefore, the crystalline size was calculated by using Scherrer's equation ($D = K\lambda/\beta\cos\theta$, where D is crystalline size, K is shape factor, β is FWHM, and θ is peak position). It was assumed that all the particles should be spherical in shape for easier comparison. According to the equation, the average particle sizes of $CuSn_{20\_min}$ before and after eCO_2R are 55 and 35 nm, respectively. Further comparison with the particle size of Cu_2O GDE films (28 nm in average) indicates that Cu_2O surface reconstructs and transforms into metallic copper on the surface during ESP. During eCO_2R, the Cu surface undergoes further reconstruction and breaks into smaller crystallites as discussed further below.

SEM-EDX results further supports the XRD analysis. As shown in Fig. 1b, the Cu_2O GDE surface has Cu_2O nanoparticles bound together by Nafion binder, and the clusters are in 30 nm to 2 μm size range. The SEM image of as-prepared $CuSn_{20\_min}$ is very different with the surface showing well-defined crystals (Fig. 1c). The Cu^0 clusters on the surface have a size range of 20–200 nm. As shown in Fig. 1d, the surface of $CuSn_{20\_min}$ reconstructs during the eCO_2R due to the weak interatomic cohesion and high surface activity of Cu at high overpotentials, which changes the particle size and morphology.[32,33] The copper particles from the surface come together to form clusters, and individual crystals are not as well-defined as before eCO_2R. It is noted that the thickness of Cu_2O film is ~8 μm and the reconstruction brings together the particles from the surface. No peaks corresponding to Sn metal or oxide were observed. However, from EDX spectra shown in Fig. 1e, Sn signal can be clearly observed on the surface of the electrodes before and after eCO_2R. Further, the Sn particles are present homogenously on the surface (Fig. S2). It is believed that due to a very small size and non-crystalline nature, SnO_2 could not be detected by XRD or SEM.

XPS, a surface sensitive technique that provides signals from first few atomic layers, can provide information about the chemical nature of different elements. The survey scans from the as-prepared samples are shown in Fig. 2a. As depicted in the figure, with the ESP duration, Sn 3 d intensity enhances, whereas Cu 2p intensity goes down. This indicates the enhancement in the surface coverage with the Sn deposition time. The samples were utilised for determining the elemental concentration on the surface. The Sn/Cu ratio for fresh $CuSn_{5\_min}$ is 2.65%, $CuSn_{20\_min}$ is 13.1% and $CuSn_{60\_min}$ is 155%. ~13% is an optimal loading of Sn on the surface for the selective eCO_2R to CO, which is also supported by another report.[18] The Sn/Cu ratio decreases for all the samples after eCO_2R, indicating the structural transformation of Sn and Cu on the surface (Table S4). There is a possibility of Sn loss in the solution which is needed to be explored by inductively coupled plasma analysis. Fig. 2b–d shows the Sn 3 d, Cu 2p and C 1s spectra from the fresh (above) and used

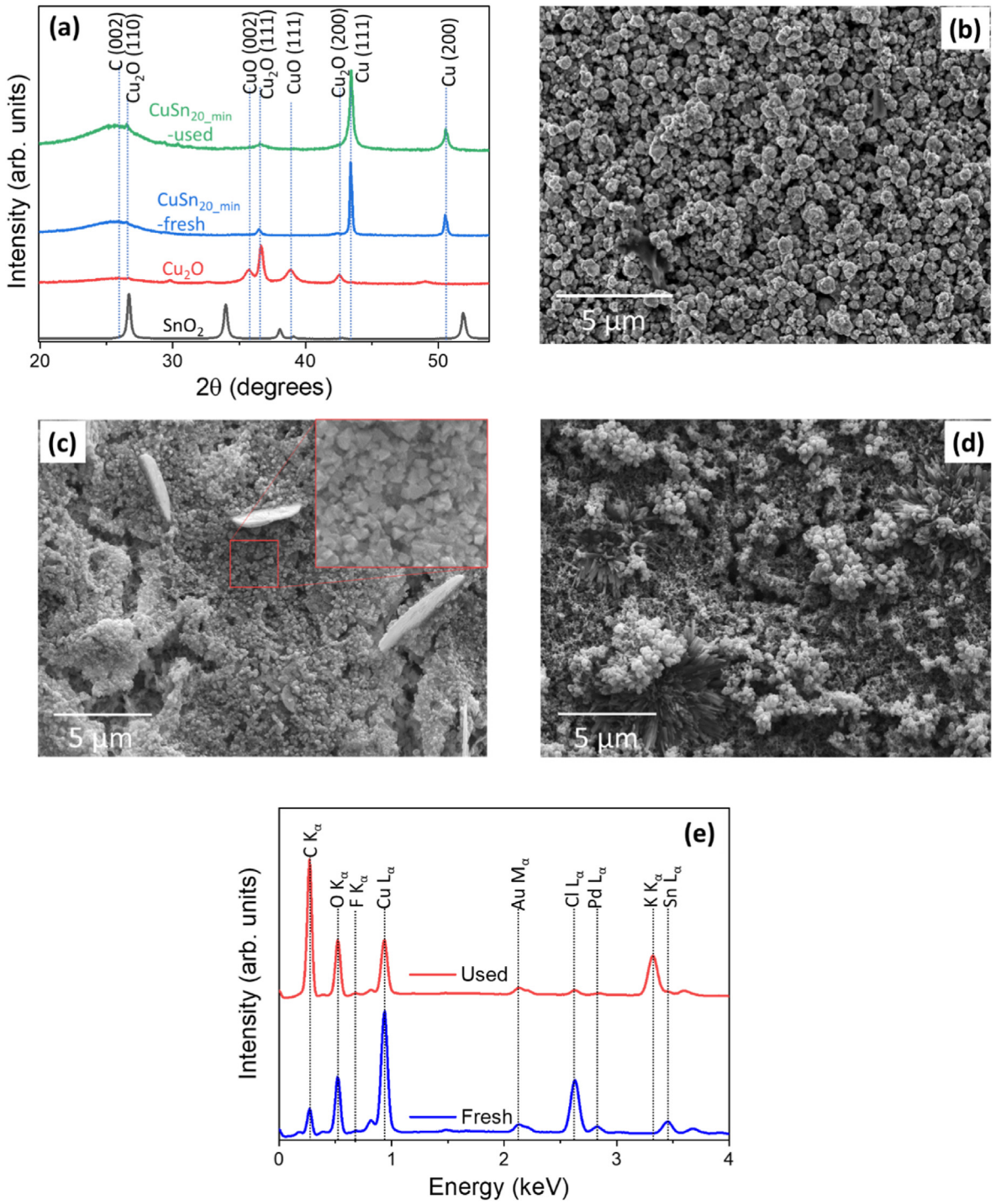

Fig. 1. (a) XRD diagram of $CuSn_{20\_min}$ sample before and after eCO_2R; Cu_2O and SnO_2 diffractograms are plotted for reference. (b) SEM image of unused Cu_2O GDE. SEM images of $CuSn_{20\_min}$ sample surface (c) before and (d) after eCO_2R reaction. (e) EDX spectra of $CuSn_{20\_min}$ sample before and after eCO_2R at −1.13 V for 1 h.

(below) $CuSn_{20\_min}$ samples. As shown in Fig. 2b, the Sn 3 d has two peaks corresponding to $Sn3d_{5/2}$ and $Sn3d_{3/2}$ at 487.3 and 495.7 eV, respectively. The peak position and FWHM (of 1.97 eV, for both) correspond to Sn oxide species.[34] After eCO_2R, the $Sn3d_{5/2}$ peak at 486.4 eV and $Sn3d_{3/2}$ peak at 494.0 eV were observed with the FWHM of 1.42 eV (same for both), which was assigned to Sn^0. The conversion of Sn oxide to Sn during eCO_2R was further corroborated by the shift in Sn_{MNN} peak kinetic energy from 423.4 to 425.2 eV (data not shown). Cu 2p XPS also show reduction of Cu species, where the fresh sample shows peaks corresponding to Cu^0 and Cu^{2+} (as labelled in Fig. 2c). From XPS, it is not possible to distinguish between Cu^0 and Cu^+, but from XRD, the major peak corresponds to Cu^0, not Cu^+. That's why it is assumed that the Cu^+ fraction of the composition is negligible. Further, from XRD, Cu^{2+} (or CuO) is absent but is a dominating species on the surface (from XPS). As XRD has much higher penetration depth (of the order of µm), it can conclude that the electrode is mostly metallic in nature with oxide presence on the surface. The surface Cu^{2+} transformation might have happened via the heat treatment by of the electrode for drying at 60 °C for 1 h. The presence of additional satellite features confirms the Cu^{2+} species. After eCO_2R, major peaks correspond to Cu metal, which was

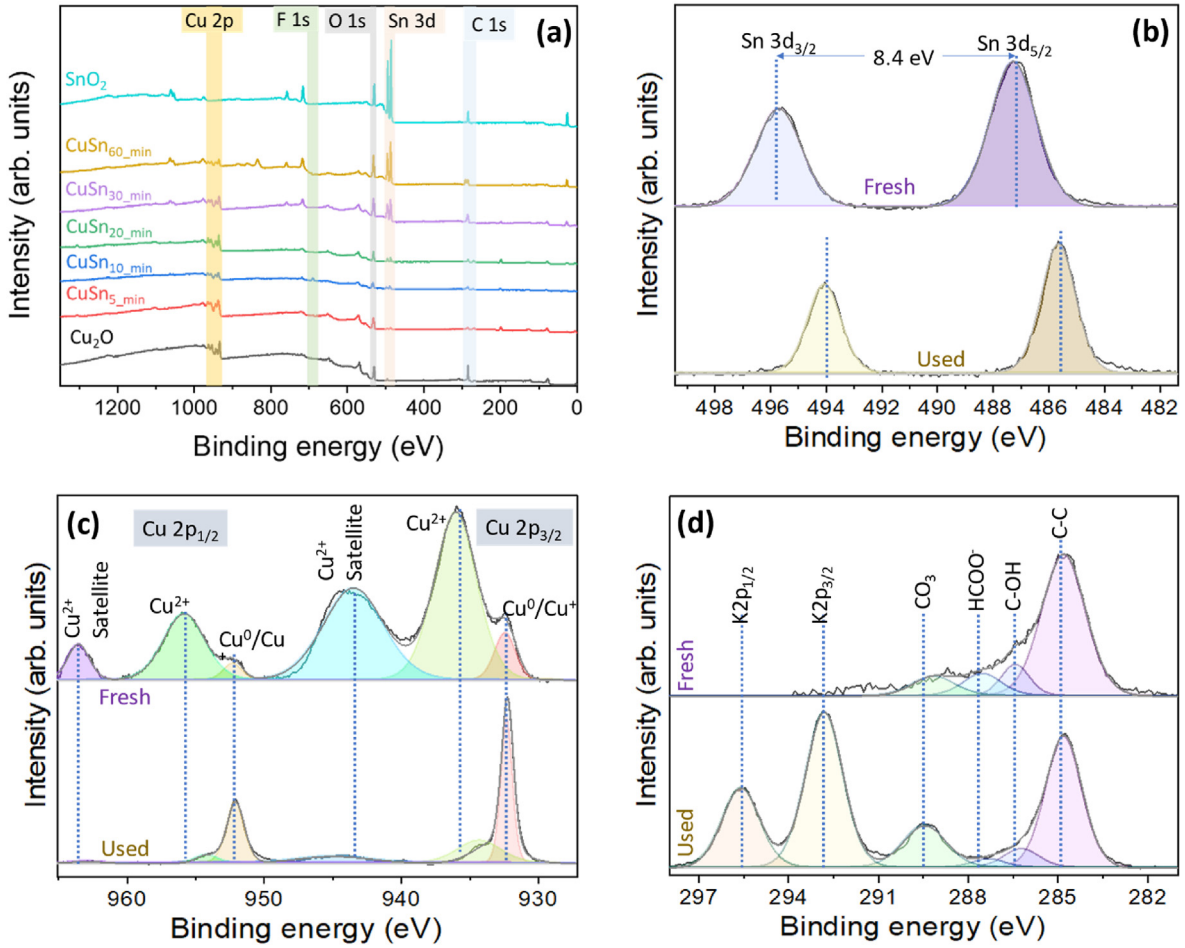

Fig. 2. (a) Survey scans of as-prepared CuSn samples. (b) Sn 3d, (c) Cu 2p and (d) C 1s spectra of $CuSn_{20\_min}$ samples before (top) and after (bottom) eCO_2R at −1.13 V for 1 h.

corroborated with XRD. The $CuSn_{20\_min}$ species had a small fraction of Cu^{2+} on the surface which has probably emerged due to drying of samples after eCO_2R in oven at 50 °C. The C 1s spectrum for the fresh $CuSn_{20\_min}$ sample had peaks which were corresponding to adventitious carbon (Fig. 2d). Nafion was absent from the surface as indicated by the absence of C–F peak (at 292.8 eV). After eCO_2R, additional peaks corresponding to K 2p (from KOH electrolyte) were identified. The area ratio of 2:1 between K $2p_{3/2}$ and $2p_{1/2}$ further confirmed the absence of C–F peak on the surface. The enhancement of CO_3 peak indicates the deposition of carbonate on the electrode surface, which is one of the mechanisms of CO_2 loss.[35] Furthermore, the combined analysis using XRD, SEM and XPS indicates that electrode surfaces have Cu and Sn species and Nafion binder is missing from them.

3.1.3. *Effect of Sn deposition time on the eCO_2R performance of CuSn*

The CV measurements were taken in −1.05 to +0.95 V vs. RHE range for 4 cycle, and the results from 3rd cycle for $CuSn_{20\_min}$ samples are shown in Fig. 3a. The CVs were recorded under N_2 and CO_2 atmosphere, sequentially. Under N_2 flow, the major peaks at 0.15 V and −0.137 V were assigned to Sn(II) to Sn reduction and Sn(IV) to Sn(II) reduction, respectively.[36,37] A minor peak at 0.5 V was also observed and was assigned to Cu(I) to Cu reduction. Under CO_2 flow, major peak corresponding to Cu(I) to Cu reduction was observed and the previously assigned Sn peaks were minor. The corresponding oxidation peaks for the materials could not be found under both N_2 and CO_2 atmosphere. This indicates the preferential reduction of oxides to the metals under the reactor conditions. The difference in the peaks between CO_2 and N_2 is believed to be due to the thin Sn layer, which have mostly reduced in the presence of N_2 and hence does not appear as a major peak in the presence of CO_2. To confirm this, the CV measurement in CO_2 environment on a fresh sample was carried out. Peaks missing in the $CuSn_{20\_min}$ sample for CO_2 CV after N_2 CV are now present. Further, CV on $CuSn_{1\_min}$ sample is also shown. The presence of relatively stronger $Cu(I)/Cu^0$ peak and absence of Sn related peaks indicate the domination of Cu species on the surface. Another factor for higher $Cu(I)/Cu^0$ peak intensity could be that for 1 min sample, and Cu_2O have been only partially reduced on the surface which reduces further during CV. The higher current in CO_2 atmosphere suggests a faster kinetics for CO_2 reduction.

Fig. 3b shows the normalised FE (%) for the various Cu–Sn GDE samples at −1.13 V. The FE for SnO_2 and Cu_2O GDEs are shown for reference. As shown in the figure, SnO_2 is selective towards the production of formate, and Cu_2O is able to produce multicarbons. These results tally with a variety of the literature reports,[2,22] listed in Table S2. Upon addition of Sn on the Cu_2O GDE surface, the product distribution changes significantly. For instance, the $CuSn_{5\_min}$ sample showed only H_2, CO, $HCOO^-$ and C_2H_4 as the majority products, different from Cu_2O. Upon further enhancement of the Sn loading, no ethylene was detected for the CuSn samples, with CO, H_2 and $HCOO^-$ being the only detected products.

Further, the current densities during the operation (shown in Table S1), were in 100–120 mA cm^{-2} range for CuSn samples with $CuSn_{20\_min}$ showing current density of 120 mA cm^{-2}. The reason for 20 min sample showing the highest current density is believed to be the faster/preferred kinetics for CO production, and similar results were

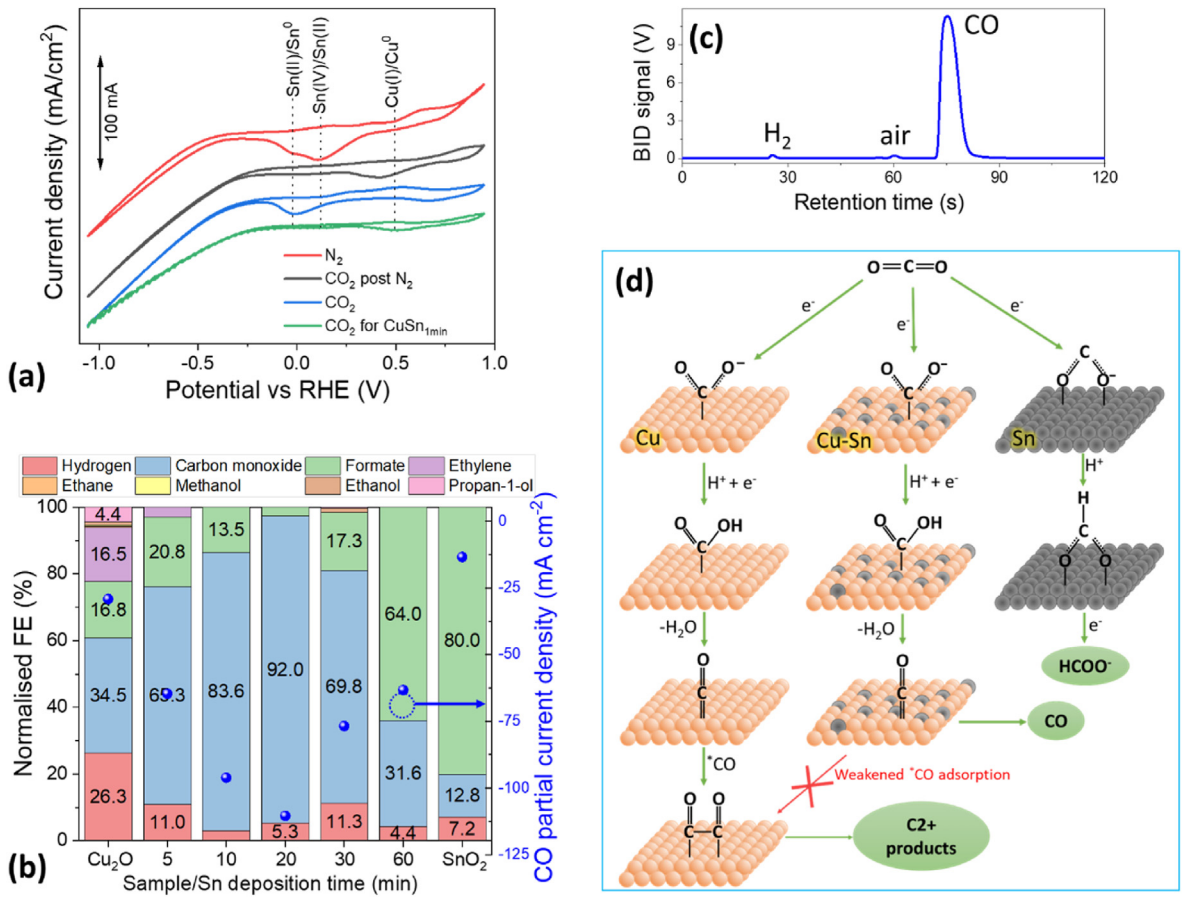

Fig. 3. (a) Cyclic voltammetry curves of $CuSn_{20\_min}$ sample under N_2 and CO_2 flow, sequentially. The CV curves of $CuSn_{20\_min}$ and $CuSn_{1\_min}$ samples are shown for comparison. The measurements were performed in −0.95 to 1.05 V range using 1 M KOH electrolyte. (b) Faradaic efficiencies of products and CO partial current densities for various CuSn samples at −1.13 V. Product distribution from Cu_2O and SnO_2 samples is shown for comparison. (c) Gas chromatogram from $CuSn_{20\_min}$ sample during eCO_2R at −1.13 V. (d) Pathways for major products for Cu–Sn, Cu and Sn electrodes.

obtained in our previous work with optimal loading sample showing highest currents.[17] The current densities for the reference samples of Cu_2O and SnO_2 were 102 and 142 mA cm^{-2}, respectively. The current densities were used to determine the partial current densities for products, and CO partial current density has been plotted in Fig. 3b, right-*y* axis. As shown in the figure, $CuSn_{20\_min}$ sample demonstrates the best performance in terms of CO Faradaic efficiency (92.0%) and CO partial current density (110.0 mA cm^{-2}). The gas chromatogram from $CuSn_{20\_min}$ is shown in Fig. 3c, and ion chromatogram is shown in Fig. S5. Upon further enhancement of the Sn loading, $HCOO^-$ FE enhances which dominates at higher Sn loading ($CuSn_{60\_min}$) and SnO_2 GDE sample.

Although there are multiple pathways and mechanisms proposed for obtaining a eCO_2R product,[2] the major pathways for the CO_2 reduction on Cu, Sn and Cu–Sn samples have been shown in Fig. 3d. The first step, which is also rate-limiting for CO_2 utilisation, is the bending and adsorption of CO_2 molecule on the catalyst surface.[38] The initial steps for the production of CO and multicarbon products are same. In the process, CO_2 gets attached to the catalyst surface by carbon atom and an electron transfer. In the next step, proton transfer results in –COOH species on the surface, which upon further attack by proton releases H_2O and stays on the surface as = C=O. For multicarbon products, another carbon (*CO) gets adsorbed in the vicinity and formation on C–C eventually leads to multi-carbon products on Cu surface.[39] However, on the Sn modified Cu sample, the *CO adsorption energy is reduced which results in CO desorbing as a product.[28,40] So, for the optimal system ($CuSn_{20\_min}$ in this case), CO would be the major product. Upon sub-optimal loading, more Cu sites are exposed, and not enough Sn close by to optimally influence the product selectivity towards CO. At higher loading (>20 min Sn deposition in the present system), due to presence of additional Sn sites, the selectivity shifts towards formate. A similar behaviour was observed for Cu–In electrodes prepared by electrochemical precipitation method in a previous investigation, where at low EPS time, along with CO, ethylene was also produced and at higher ESP time, formate started to contribute heavily.[23] So, the optimisation of Sn loading and its interaction with Cu is vital for the selective CO production from eCO_2R. For the eCO_2R to $HCOO^-$, the terminal oxygen atoms are bound to the surface of the catalyst with an e^- transfer. In the next step, a proton transfer to the carbon atom takes place which promotes the desorption of HCOO* followed by electron transfer to obtain $HCOO^-$ in solution. For H_2 evolution, surface bound protons are attacked by a second proton, and H_2 evolution takes place.

3.2. *Product selectivity over time for $CuSn_{20\_min}$*

For determining the selectivity at fixed potential, $CuSn_{20\_min}$ sample was kept at −1.13 V. The change in product distribution and current density over time for sample at −1.13 V is shown in Fig. 4a. CO FE reduces overtime from 91.8% to 47.1%, while H_2 FE enhances from 5% to 50.6% over time. Formate FE also decreased over time from 3.2% to 2.2%. Soon after 3 h, the reactor flooded (the catholyte crossed over from cathode chamber to gas chamber), and GC sampling was stopped. The current vs. time plot at fixed potential of −1.13 V is shown in Fig. 4b. The prominent mechanism of reactor flooding in the alkaline systems is the formation of carbonate or bicarbonate salts in the GDE structure which

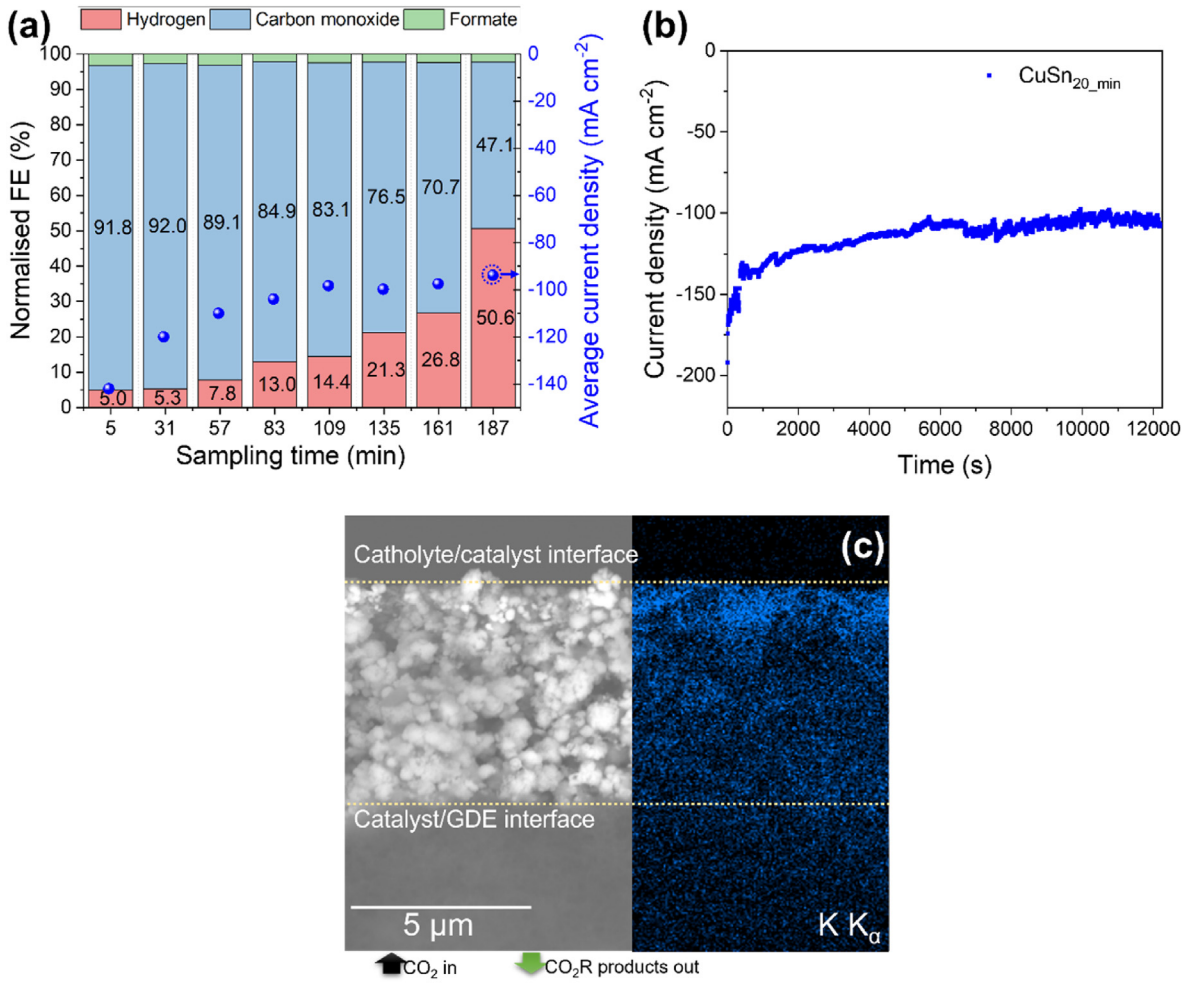

Fig. 4. (a) Change in product FEs and CO partial current density (*y*-axis, right) over time and, (b) Current vs. time for $CuSn_{20\_min}$ electrode at −1.13 V. (c) Cross-sectional SEM-EDX of $CuSn_{20\_min}$ after eCO_2R.

changes the hydrophobicity of the GDE.[41] Another mechanism is the change in the hydrophobicity of carbon GDE at higher overpotentials due to hydrogen evolution at GDE support sites along with catalyst.[42] Experimental confirmation of the reactor flooding was obtained by performing the cross-section SEM-EDX of the GDE electrode post eCO_2R. Fig. 4c shows the cross-sectional SEM image and corresponding K K_α EDX map of $CuSn_{20\_min}$ GDE. Because KOH electrolyte is the only source of K, the K_α elemental map should represent the extent of electrolyte-electrode interaction. As shown in the figure, the K is present beyond the catalyst later and can be observed in the microporous layer. This indicates the flooding of the electrolyte from catalyst to the GDE support. The enhancement in the H_2 FE when electrolyte creeps into the GDE paper has been observed by other authors and results from electrolyte creeping, and the electrolyte-electrode-gas interface shifts to the carbon paper away from the catalysts.[43] Carbon paper has hydrogen as predominant product as shown in Fig. S6, and that's why the H_2 FE enhances when the interface shifts away from catalyst. Also, the average current density of carbon GDE paper during the eCO_2R is 41 mA cm^{-2}. The cathodic current density also decreases overtime and in first 3 h it drops from 142 to 94 mA cm^{-2}, a 33% decrease. The decrease in the current density is also indicative of the shift of the reaction interface to carbon GDE rather than change in the intrinsic activity of the catalyst.

While the selectivity towards CO has been significantly improved using inexpensive and abundant CuSn based electrodes, the low stability is still a significant challenge. For eCO_2R to be economically viable, the stability target is > 50,000 h, CO_2 utilisation efficiency of 90%–100%, energy efficiency of >50%, and the system should be operable at industrially relevant current density of >300 mA cm^{-2}[44] The system demonstrated in the current work is stable for 3 h during operation, has CO_2 utilisation efficiency of ~7%, has energy efficiency of 45%, and delivers a current density of 120 mA cm^{-2}. Even though the current is one of the highest ever reported for Cu–Sn systems, it is still far from the commercialisation target (Table S2). However, the areas which need most attention for realising the commercialisation potential is improving the GDE stability and drawing higher current out of the system. For the further improvement in the intrinsic activity of the catalysts, novel nano structures should be tested, and catalysts should also be investigated using in-situ characterisation techniques for improved structure-activity correlation and mechanistic understanding. The novel catalysts of 2D heterostructures like MoS_2 and MXenes are potential candidates for enhanced performance of the electrocatalysts by either forming heterostructures or utilising them as catalyst support.[45,46] Regarding advancing the GDE reactor stability, one approach can be to manage flooding and recirculating the flooded electrolyte. For instance, Jeanty et al. used a Ag GDE in three-chamber reactor and observed flooding after 30 min of reactor operation.[11] By capturing the water coming out on the other side of GDE and continuing to operate the GDE, they were able to keep the reactor running at 150 mA cm^{-2} for hundreds of hours with >60% CO Faradaic efficiency. Along with trying out novel reactor designs, the GDE electrode stability and structural integrity should also be improved.[47] GDE electrodes usually consist of carbon fibre support layer which have a top microporous layer and PTFE coating to improve hydrophobicity. On

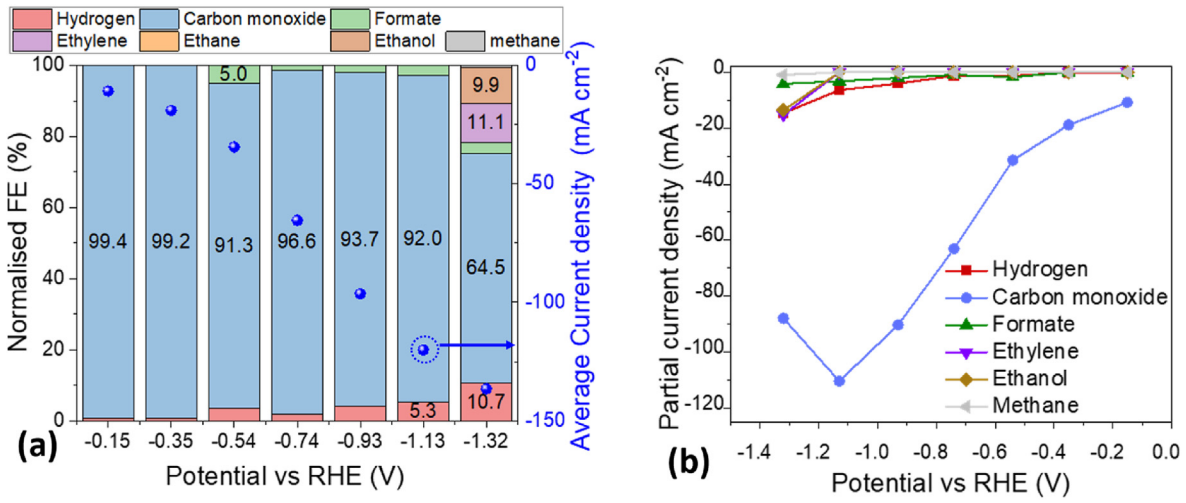

Fig. 5. (a) Variation of FEs and current densities at different potentials and, (b) partial current densities of the products for $CuSn_{20\_min}$ samples.

the top of GDE paper, catalyst material with a binder is added which works as the active electrode. There are opportunities to improve the GDE stability by improving the microporous layer and catalyst binder. As catalyst/binder is the first line of defence against flooding, the degradation of binder can make the metal leach in the electrolyte or change the hydrophobicity of the layer.[48] Xing et al. based on testing a series of binders deduced that PTFE was a better binder as it did not change the electrode hydrophobicity much (contact angle change from 150° to 144° after eCO_2R at 250 mA cm^{-2}) and delivered stable performance.[49] Carbonaceous catalyst support and microporous layers present opportunities for the enhancement in the catalyst activity and stability.[50] We have some ongoing experiments on the stability of the GDE improvement by engineering binder and microporous layers.

3.3. *Effects of applied potential for CO_2 reduction on $CuSn_{20\_min}$*

Fig. 5a shows the product distribution for $CuSn_{20\_min}$ samples at various potentials in −0.15 to −1.32 V range. The product distribution largely remained the same except at −1.32 V, where ethylene and ethanol were also observed. Upon closer look, it is observed that the CO FE% decreases slightly to 92% at −1.13 V with the enhancement in the cathodic potential from the highest value of 99.4%. It is because at higher cathodic potentials, higher current is drawn out of system and availability of CO_2 at the interface becomes a limiting factor at higher current, which is compensated by the higher hydrogen production even though it may not be a thermodynamically favourable reaction. The cathodic current density, as expected, enhanced from −10.8 to −136.4 mA cm^{-2} upon increasing in the cathodic potential from −0.15 to −1.32 V. The values of partial current densities for H_2, CO and $HCOO^-$ at various potentials have been shown in Fig. 5b. As expected, the FEs for CO and $HCOO^-$ enhance, even though there is higher H_2 production. At −1.32 V, the decrease in the CO partial current density is due to the production of other CO_2 reduction products. Henceforth, the higher utilisation of CO_2 at −1.32 V is not reflected in the CO partial current density. The change in product selectivity towards higher carbon at high overpotentials have been observed by other researchers also.[28,51,52] For instance, Kim et al. using electropolished Cu electrode obtained only CO, H_2 and HCOOH as the products[52] in −0.5 to −0.8 V vs. RHE range. In the potential range of −0.9 to −1.2 V vs. RHE, additional products of CH_4, C_2H_4, C_2H_5OH, C_3H_7OH were observed, which became dominant at > 1.0 V vs. RHE, depicting the potential dependant FEs of the products.

4. Conclusions

Sn modified Cu_2O GDEs have delivered selective CO production via electrochemical CO_2 reduction. The Cu_2O GDE with 20 min Sn ESP ($CuSn_{20\_min}$) sample demonstrated the highest CO FE of 92% and highest CO patrial current density of 110 mA cm^{-2} at −1.15 V vs. RHE. The electrocatalyst showed stable performance at various potentials in −0.15 to −1.35 V vs. RHE range. CO, $HCOO^-$ and H_2 were the only products obtained at lower potentials till −1.15 V, with ethylene and ethanol being the additional products at −1.35 V. The GDE electrocatalyst showed stable performance for >3 h at fixed potential of −1.15 V vs. RHE. It is demonstrated experimentally that flooding of the reactor hinders the reactor operation for longer durations. XRD and SEM analyses indicates the change in crystalline nature of Cu_2O by reduction to Cu. After eCO_2R, the nature of Cu GDE remains the same, but the crystallite size reduces from 55 to 35 nm. From XPS, pristine CuSn has Sn in the oxide form which reduces to Sn metal during the CO_2 reduction. Overall, this study demonstrates the potential of CuSn binary electrocatalysts for selective CO_2R to CO production at high current densities.

Declaration of competing interest

The authors declare that they have no known competing financial interests or personal relationships that could have appeared to influence the work reported in this paper.

Acknowledgement

The authors would like to acknowledge the support from the UKRI Interdisciplinary Centre for Circular Chemical Economy (EP/V011863/1), EPSRC LifesCO2R project (EP/N009746/1 EP/N009746/2) and EPSRC NECEM Energy Material Centre (EP/R021503/1). Loughborough Materials Characterisation Centre Pump Prime grant which enabled the access to the characterisation facilities is also acknowledged.

Appendix A. Supplementary data

Supplementary data to this article can be found online at https://doi.org/10.1016/j.matre.2023.100196.

References

1. Gabrielli P, Gazzani M, Mazzotti M. The role of carbon capture and utilization, carbon capture and storage, and biomass to enable a net-zero-CO_2 emissions chemical industry. *Ind Eng Chem Res*. 2020;59:7033–7045. https://doi.org/10.1021/ACS.IECR.9B06579/ASSET/IMAGES/LARGE/IE9B06579_0004.JPEG.
2. Nitopi S, Bertheussen E, Scott SB, et al. Progress and perspectives of electrochemical CO_2 reduction on copper in aqueous electrolyte. *Chem Rev*. 2019;119:7610–7672. https://doi.org/10.1021/acs.chemrev.8b00705.
3. Stephens IEL, Chan K, Bagger A, et al. Roadmap on low temperature electrochemical CO_2 reduction. *J Phys Energy*. 2022;4, 042003. https://doi.org/10.1088/2515-7655/ac7823, 2022.
4. Gawel A, Jaster T, Siegmund D, et al. Electrochemical CO_2 reduction - the macroscopic world of electrode design, reactor concepts & economic aspects. *iScience*. 2022;25, 104011. https://doi.org/10.1016/J.ISCI.2022.104011.
5. Li D, Zhang H, Xiang H, et al. How to go beyond C1products with electrochemical reduction of CO_2. *Sustain Energy Fuels*. 2021;5:5893–5914. https://doi.org/10.1039/d1se00861g.
6. Xiang H, Rasul S, Scott K, Portoles J, Cumpson P, Yu EH. Enhanced selectivity of carbonaceous products from electrochemical reduction of CO_2 in aqueous media. *J CO_2 Util*. 2019;30:214–221. https://doi.org/10.1016/j.jcou.2019.02.007.
7. Zhong J, Yang X, Wu Z, Liang B, Huang Y, Zhang T. State of the art and perspectives in heterogeneous catalysis of CO_2 hydrogenation to methanol. *Chem Soc Rev*. 2020;49:1385–1413. https://doi.org/10.1039/c9cs00614a.
8. Höök M, Fantazzini D, Angelantoni A, Snowden S. Hydrocarbon liquefaction: viability as a peak oil mitigation strategy. *Philos Trans R Soc A Math Phys Eng Sci*. 2014;372, 20120319. https://doi.org/10.1098/RSTA.2012.0319.
9. Nattestad A, Wagner K, Wallace GG. Scale up of reactors for carbon dioxide reduction. *Front Chem Sci Eng*. 2022. https://doi.org/10.1007/s11705-022-2178-7.
10. Ozden A, Wang Y, Li F, et al. Cascade CO_2 electroreduction enables efficient carbonate-free production of ethylene. *Joule*. 2021;5:706–719. https://doi.org/10.1016/J.JOULE.2021.01.007.
11. Jeanty P, Scherer C, Magori E, Wiesner-Fleischer K, Hinrichsen O, Fleischer M. Upscaling and continuous operation of electrochemical CO_2 to CO conversion in aqueous solutions on silver gas diffusion electrodes. *J CO_2 Util*. 2018;24:454–462. https://doi.org/10.1016/J.JCOU.2018.01.011.
12. Subramanian S, Athira KR, Anbu Kulandainathan M, Senthil Kumar S, Barik RC. New insights into the electrochemical conversion of CO_2 to oxalate at stainless steel 304L cathode. *J CO2 Util*. 2020;36:105–115. https://doi.org/10.1016/J.JCOU.2019.10.011.
13. Monteiro MCO, Philips MF, Schouten KJP, Koper MTM. Efficiency and selectivity of CO_2 reduction to CO on gold gas diffusion electrodes in acidic media. *Nat Commun*. 2021:1–7. https://doi.org/10.1038/s41467-021-24936-6, 121 2021;12.
14. Duan X, Xu J, Wei Z, et al. Metal-free carbon materials for CO_2 electrochemical reduction. *Adv Mater*. 2017;29, 1701784. https://doi.org/10.1002/ADMA.201701784.
15. Tian Z, Dong C, Yu Q, et al. A universal nanoreactor strategy for scalable supported ultrafine bimetallic nanoparticles synthesis. *Mater Today*. 2020;40:72–81. https://doi.org/10.1016/J.MATTOD.2020.05.017.
16. Wu J, Ma S, Sun J, et al. A metal-free electrocatalyst for carbon dioxide reduction to multi-carbon hydrocarbons and oxygenates. *Nat Commun*. 2016 71 2016;7:1–6. https://doi.org/10.1038/ncomms13869.
17. Xiang H, Rasul S, Hou B, Portoles J, Cumpson P, Yu EH. Copper-indium binary catalyst on a gas diffusion electrode for high-performance CO_2 electrochemical reduction with record CO production efficiency. *ACS Appl Mater Interfaces*. 2020;12:601–608. https://doi.org/10.1021/acsami.9b16862.
18. Pardo Pérez LC, Arndt A, Stojkovikj S, et al. Determining structure-activity relationships in oxide derived Cu-Sn catalysts during CO_2 electroreduction using X-ray spectroscopy. *Adv Energy Mater*. 2022;12. https://doi.org/10.1002/AENM.202103328.
19. Jeon HS, Timoshenko J, Scholten F, et al. Operando insight into the correlation between the structure and composition of CuZn nanoparticles and their selectivity for the electrochemical CO_2 reduction. *J Am Chem Soc*. 2019;141:19879–19887. https://doi.org/10.1021/jacs.9b10709, 2019.
20. Yin C, Li Q, Zheng J, et al. Progress in regulating electronic structure strategies on Cu-based bimetallic catalysts for CO_2 reduction reaction. *Adv Powder Mater*. 2022;1, 100055. https://doi.org/10.1016/J.APMATE.2022.100055.
21. Sarfraz S, Garcia-Esparza AT, Jedidi A, Cavallo L, Takanabe K. Cu−Sn bimetallic catalyst for selective aqueous electroreduction of CO_2 to CO. *ACS Catal*. 2016;6:2842–2851. https://doi.org/10.1021/acscatal.6b00269.
22. Rasul S, Pugnant A, Yu E. Electrochemical reduction of CO_2 at multi-metallic interfaces. *ECS Trans*. 2018;85:57–66. https://doi.org/10.1149/08510.0057ecst.
23. Xiang H, Miller HA, Bellini M, et al. Production of formate by CO_2 electrochemical reduction and its application in energy storage. *Sustain Energy Fuels*. 2019;4:277–284. https://doi.org/10.1039/c9se00625g.
24. Harmon NJ, Wang H. Electrochemical CO_2 reduction in the presence of impurities: influences and mitigation strategies. *Angew Chem Int Ed*. 2022;61, e202213782. https://doi.org/10.1002/ANIE.202213782.
25. Zhao Y, Wang C, Wallace GG. Tin nanoparticles decorated copper oxide nanowires for selective electrochemical reduction of aqueous CO_2 to CO. *J Mater Chem*. 2016;4:10710–10718. https://doi.org/10.1039/c6ta04155h.
26. Dong WJ, Lim JW, Hong M, et al. Evidence of local corrosion of bimetallic Cu−Sn catalysts and its effects on the selectivity of electrochemical CO_2 reduction. *Cite This ACS Appl Energy Mater*. 2020. https://doi.org/10.1021/acsaem.0c01617, 10568–77.
27. Yoo CJ, Dong WJ, Park JY, et al. Compositional and geometrical effects of bimetallic Cu-Sn catalysts on selective electrochemical CO_2 reduction to CO. *ACS Appl Energy Mater*. 2020;3:4466–4473. https://doi.org/10.1021/acsaem.0c00157.
28. Gao J, Li J, Liu Y, et al. Solar reduction of carbon dioxide on copper-tin electrocatalysts with energy conversion efficiency near 20. *Nat Commun*. 2022:1–11. https://doi.org/10.1038/s41467-022-33049-7, 131 2022;13.
29. Tan X, Guo W, Liu S, et al. A Sn-stabilized Cu d+ electrocatalyst toward highly selective CO_2-to-CO in a wide potential range. *Chem Sci*. 2022;13:11918–11925. https://doi.org/10.1039/d2sc04607e.
30. Ju W, Jiang F, Ma H, et al. Electrocatalytic reduction of gaseous CO_2 to CO on Sn/Cu-Nanofiber-Based gas diffusion electrodes. *Adv Energy Mater*. 2019;9, 1901514. https://doi.org/10.1002/AENM.201901514.
31. Li F, Thevenon A, Rosas-Hernández A, et al. Molecular tuning of CO_2-to-ethylene conversion. *Natalia*. 2019;577:509–513. https://doi.org/10.1038/s41586-019-1782-2.
32. Arán-Ais RM, Rizo R, Grosse P, et al. Imaging electrochemically synthesized Cu_2O cubes and their morphological evolution under conditions relevant to CO2 electroreduction. *Nat Commun*. 2020;11:3489. https://doi.org/10.1038/s41467-020-17220-6.
33. Kim Y-G, Hess Baricuatro J, Javier A, Gregoire JM, Soriaga MP. The evolution of the polycrystalline copper surface, first to Cu(111) and then to Cu(100), at a fixed CO_2RR potential: a study by operando EC-STM. *Langmuir*. 2014;30:15053–15056. https://doi.org/10.1021/la504445g.
34. Moulder JF, Stickle WF, Sobol PE, Bomben KD. *Handbook of X-Ray Photoelectron Spectroscopy*. Eden Prairie, MN: Perkin-Elmer; 1992.
35. Rabinowitz JA, Kanan MW. The future of low-temperature carbon dioxide electrolysis depends on solving one basic problem. *Nat Commun*. 2020;11:5231. https://doi.org/10.1038/s41467-020-19135-8.
36. Rasul S, Pugnant A, Xiang H, Fontmorin JM, Yu EH. Low cost and efficient alloy electrocatalysts for CO_2 reduction to formate. *J CO2 Util*. 2019;32:1–10. https://doi.org/10.1016/j.jcou.2019.03.016.
37. Nakayama S, Sugihara T, Matsumoto J, Notoya T, Osakai T. Chemical state analysis of tin oxide films by voltammetric reduction. *J Electrochem Soc*. 2011;158:C341. https://doi.org/10.1149/1.3622345.
38. Wang S, Kou T, Baker SE, Duoss EB, Li Y. Recent progress in electrochemical reduction of CO_2 by oxide-derived copper catalysts. *Mater Today Nano*. 2020;12, 100096. https://doi.org/10.1016/J.MTNANO.2020.100096.
39. Jaster T, Gawel A, Siegmund D, et al. Electrochemical CO_2 reduction toward multicarbon alcohols - the microscopic world of catalysts & process conditions. *iScience*. 2022;25, 104011. https://doi.org/10.1016/J.ISCI.2022.104010.
40. Pardo Pérez LC, Arndt A, Stojkovikj S, et al. Determining structure-activity relationships in oxide derived Cu-Sn catalysts during CO_2 electroreduction using X-ray spectroscopy. *Adv Energy Mater*. 2022;12, 2103328. https://doi.org/10.1002/aenm.202103328.
41. Sharma PK, Cortes MALRM, Hamilton JWJ, Han Y, Byrne JA, Nolan M. Surface modification of TiO_2 with copper clusters for band gap narrowing. *Catal Today*. 2019;321–322:9–17. https://doi.org/10.1016/j.cattod.2017.12.002.
42. Yang K, Kas R, Smith WA, Burdyny T. Role of the carbon-based gas diffusion layer on flooding in a gas diffusion electrode cell for electrochemical CO_2 reduction. *ACS Energy Lett*. 2021;6:40. https://doi.org/10.1021/acsenergylett.0c02184.
43. Kong Y, Hu H, Liu M, et al. Visualisation and quantification of flooding phenomena in gas diffusion electrodes used for electrochemical CO_2 reduction: a combined EDX/ICP–MS approach. *J Catal*. 2022;408:1–8. https://doi.org/10.1016/J.JCAT.2022.02.014.
44. Kibria MG, Edwards JP, Gabardo CM, et al. Electrochemical CO_2 reduction into chemical feedstocks: from mechanistic electrocatalysis models to system design. *Adv Mater*. 2019;31, 1807166. https://doi.org/10.1002/ADMA.201807166.
45. Chen X, Ma C, Tan Z, et al. One-dimensional screw-like MoS_2 with oxygen partially replacing sulfur as an electrocatalyst for the N_2 reduction reaction. *Chem Eng J*. 2022;433, 134504. https://doi.org/10.1016/J.CEJ.2022.134504.
46. Chen X, Zhang S, Qian X, et al. Enabling efficient electrocatalytic conversion of N_2 to NH_3 by Ti_3C_2 MXene loaded with semi-metallic 1T′-MoS_2 nanosheets. *Appl Catal B Environ*. 2022;310, 121277. https://doi.org/10.1016/J.APCATB.2022.121277.
47. Siritanaratkul B, Forster M, Greenwell F, Sharma PK, Yu EH, Cowan AJ. Zero-gap bipolar membrane electrolyzer for carbon dioxide reduction using acid-tolerant molecular electrocatalysts. *J Am Chem Soc*. 2022;144:7551–7556. https://doi.org/10.1021/jacs.1c13024.
48. Nwabara UO, Hernandez AD, Henckel DA, et al. Binder-focused approaches to improve the stability of cathodes for CO_2 electroreduction. *Cite This ACS Appl Energy Mater*. 2021;2021:5175–5186. https://doi.org/10.1021/acsaem.1c00715.
49. Xing Z, Hu L, Ripatti DS, Hu X, Feng X. Enhancing carbon dioxide gas-diffusion electrolysis by creating a hydrophobic catalyst microenvironment. *Nat Commun*. 2021;12:136. https://doi.org/10.1038/s41467-020-20397-5.
50. Wu Y, Garg S, Li M, et al. Effects of microporous layer on electrolyte flooding in gas diffusion electrodes and selectivity of CO_2 electrolysis to CO. *J Power Sources*. 2022;522, 230998. https://doi.org/10.1016/J.JPOWSOUR.2022.230998.
51. Kim D, Kley CS, Li Y, Yang P. Copper nanoparticle ensembles for selective electroreduction of CO_2 to C2–C3 products. *Proc Natl Acad Sci U S A*. 2017;114:10560–10565. https://doi.org/10.1073/PNAS.1711493114/-/DCSUPPLEMENTAL/PNAS.1711493114.SAPP.PDF.
52. Kim T, Palmore GTR. A scalable method for preparing Cu electrocatalysts that convert CO_2 into C2+ products. *Nat Commun*. 2020;11:3622. https://doi.org/10.1038/s41467-020-16998-9.

Preetam Kumar Sharma is a postdoctoral research associate in electrochemical CO_2 utilisation at Loughborough University, UK. He obtained his Ph.D. in solar fuels from Ulster University, UK. His current research interests are developing electrochemical technologies for CO_2 utilisation, water splitting and generating resources from waste.

Eileen Yu holds a Chair of Electrochemical Engineering in the Department of Chemical Engineering, Loughborough University, UK. She obtained her Ph.D. from Newcastle University pioneering on the development of direct methanol alkaline fuel cells. She has a wide range of experience in various fields in electrochemical and bioelectrochemical systems for energy, environmental and biomedical applications. Her current research includes understanding fundamentals and engineering applications of electrocatalysis and microbial electrosynthesis for CO_2 utilisation, resource recovery from wastes, and bioremediation and environment monitoring with bioelectrochemical systems.